

Terrestrial Planet Optical Phase Curves. I. Direct Measurements of the Earth

De Cock, Roderick; Livengood, Timothy A.; Stam, Daphne M.; Lisse, Carey M.; Hewagama, Tilak; Deming, L. Drake

DOI

[10.3847/1538-3881/ac3234](https://doi.org/10.3847/1538-3881/ac3234)

Publication date

2022

Document Version

Final published version

Published in

Astronomical Journal

Citation (APA)

De Cock, R., Livengood, T. A., Stam, D. M., Lisse, C. M., Hewagama, T., & Deming, L. D. (2022). Terrestrial Planet Optical Phase Curves. I. Direct Measurements of the Earth. *Astronomical Journal*, 163(1), Article 5. <https://doi.org/10.3847/1538-3881/ac3234>

Important note

To cite this publication, please use the final published version (if applicable).
Please check the document version above.

Copyright

Other than for strictly personal use, it is not permitted to download, forward or distribute the text or part of it, without the consent of the author(s) and/or copyright holder(s), unless the work is under an open content license such as Creative Commons.

Takedown policy

Please contact us and provide details if you believe this document breaches copyrights.
We will remove access to the work immediately and investigate your claim.



Terrestrial Planet Optical Phase Curves. I. Direct Measurements of the Earth

Roderick De Cock¹ , Timothy A. Livengood^{2,3} , Daphne M. Stam¹ , Carey M. Lisse⁴ , Tilak Hewagama³, and L. Drake Deming^{2,5}

¹ Aerospace Engineering Department, Technical University Delft Delft, The Netherlands; roderickdecock@gmail.com

² Department of Astronomy, University of Maryland, College Park, MD USA

³ Center for Research and Exploration in Space Science and Technology, NASA/GSFC, Greenbelt, MD USA

⁴ Johns Hopkins University Applied Physics Laboratory, Laurel, MD USA

⁵ NASA Astrobiology Institute's Virtual Planetary Laboratory, USA

Received 2021 August 27; revised 2021 October 12; accepted 2021 October 20; published 2021 December 10

Abstract

NASA's EPOXI mission used the Deep Impact spacecraft to observe the disk-integrated Earth as an analog to terrestrial exoplanets' appearance. The mission took five 24 hr observations in 2008–2009 at various phase angles (57° – 86°) and ranges (0.11–0.34 au), of which three equatorial (E1, E4, E5) and two polar (P1, North and P2, South). The visible data taken by the HRIV instrument ranges from 0.3 to 1.0 μm , taken through seven spectral filters that have spectral widths of about 100 nm, and which are centered about 100 nm apart, from 350 to 950 nm. The disk-integrated, 24 hr averaged signal is used in a phase angle analysis. A Lambertian-reflecting, spherical planet model is used to estimate geometric albedo for every observation and wavelength. The geometric albedos range from 0.143 (E1, 950 nm) to 0.353 (P2, 350 nm) and show wavelength dependence. The equatorial observations have similar values, while the polar observations have higher values due to the ice in view. Therefore, equatorial observations can be predicted for other phase angles, but (Earth-like) polar views (with ice) would be underestimated.

Unified Astronomy Thesaurus concepts: [Earth \(planet\) \(439\)](#); [Phase angle \(1217\)](#); [Optical astronomy \(1776\)](#); [Exoplanets \(498\)](#); [Observational astronomy \(1145\)](#)

1. Introduction

After almost three decades of exoplanet discoveries, we now know that possibly up to 50% of solar-type stars have a small, terrestrial-type planet in its habitable zone (Bryson et al. 2020). However, even though we know such small, potentially habitable planets are out there, little is known about the properties of their atmospheres, surface, climate, and with that, their habitability. To obtain such information on small planets in the habitable zones of solar-type stars, direct observations of the visible to near-infrared starlight that these planets reflect and/or the thermal radiation that these planets emit should be measured. Except for planets around the nearest stars, which might be imaged by large ground-based telescopes such as the European Extremely Large Telescope, such measurements would require dedicated space telescopes beyond current capabilities.

Space telescopes that could perform these measurements are being proposed and designed with specific interest in exoplanet observations. The Habitable Exoplanet Observatory (Habex) proposed mission focuses on habitable zone Earth-like planets around Sun-like stars. The various instruments would cover a wavelength range from ultraviolet 0.115 μm to near-infrared 1.8 μm (Gaudi et al. 2020). The Large UV/Optical/IR Surveyor (LUVOIR) is another proposed mission that will have the capabilities to observe and characterize a more diverse range of exoplanets. It will have a wavelength range from 0.1 to 2.5 μm (The LUVOIR Team 2019). Both these missions show the interest in exoplanets and the desire to have space

telescopes committed to this topic. They are also pushing the technological limits, Habex, by using a free-flying starshade as an external occulter and LUVOIR by using very a large telescope. These missions will only fly by the end of the next decade (\sim 2040). By then, the Earth's appearance as a model exoplanet (and its dominant factors) must be well understood to compare with results and interpret conditions on spatially unresolved exoplanets.

Even at this time, only a disk-integrated signal can be anticipated. Most Earth observation data comes from near-Earth/Earth orbiting spacecraft (NASA EODIS, ESA GMES; Pfeifer et al. 2012; Aschbacher & Milagro-Pérez 2012; Kansakar & Hossain 2016). Those data are often highly detailed, large volume and recreating Earth exoplanet-like data can be very tedious as it entails data reduction/selection, numerical modeling to reconstruct a simulated view of the whole disk from a distance and/or require special treatments (data gaps, spacecraft maneuvers; Hearty et al. 2009; Robinson et al. 2011; Mettler et al. 2020). Certain physics important for local phenomena that maybe captured by high-resolution instruments is not significant in a full Earth observation. It is essential to simplify modeling as much as possible while retaining the greatest amount of environmental information that can be retrieved unambiguously, a task for which empirical whole-disk observations can provide essential constraints. Data from deep space is needed, capturing the full Earth. Since the distance is not large on astronomical scale, the signal-to-noise ratio is very high. This is advantageous for the analysis compared to real exoplanet observations.

The EPOXI mission took such data to allow the reconstruction of Earth as an exoplanet. The EPOXI mission was an extended mission after Deep Impact had completed its mission at 9P/Tempel 1 (Blume 2005). The extended mission included



Original content from this work may be used under the terms of the [Creative Commons Attribution 4.0 licence](#). Any further distribution of this work must maintain attribution to the author(s) and the title of the work, journal citation and DOI.

Table 1
Observational Parameters of the Five Observations (E1, E4, E5, P1, and P2) that we Analyze in this Paper

Obs.	Date	Phase Angle α	Illum. Frac. ^a f	Subobserver Latitude	Subsolar Latitude	SC-Earth Range [au]
E1	18–19 Mar '08	57°7	76.7%	1.6° N	0.4° S	0.18
E4	28–29 May '08	75°1	62.9%	0.3° S	21.7° N	0.34
E5	4–5 June '08	76°6	61.6%	0.3° N	22.6° N	0.34
P1	27–28 Mar. '09	85°9	53.6%	61.5° N	3.0° N	0.11
P2	4–5 Oct. '09	86°4	53.1%	73.7° S	4.7° S	0.11

Note. In the columns (from left to right): the observation, the date (in UTC), the phase angle α , the illuminated fraction^a f of the Earth, the subobserver latitude, the subsolar latitude, and the spacecraft-Earth range.

^a The illuminated fraction f is related to phase angle α through $f = \frac{1}{2}(1 + \cos \alpha)$ (Cowan et al. 2011).

Table 2
The Measured and Disk-integrated Reflected Fluxes for the Five Observations (E1, E4, E5, P1, and P2)

Obs.	350 nm 372 nm 365–400	450 nm 454 nm 408–496	550 nm 550 nm 497–600	650 nm 647 nm 599–697	750 nm 745 nm 699–796	850 nm 842 nm 800–892	950 nm 948 nm 898–970
E1	3.49 ± 0.12	4.94 ± 0.20	3.75 ± 0.14	3.07 ± 0.12	2.52 ± 0.13	2.22 ± 0.13	1.36 ± 0.09
E4	2.48 ± 0.15	3.61 ± 0.23	2.79 ± 0.16	2.30 ± 0.12	1.92 ± 0.11	1.70 ± 0.12	1.02 ± 0.07
E5	2.42 ± 0.11	3.53 ± 0.18	2.72 ± 0.11	2.23 ± 0.08	1.87 ± 0.10	1.66 ± 0.10	0.98 ± 0.07
P1	2.28 ± 0.11	3.59 ± 0.18	2.86 ± 0.11	2.43 ± 0.08	2.04 ± 0.06	1.79 ± 0.06	1.14 ± 0.04
P2	2.32 ± 0.10	3.73 ± 0.18	3.00 ± 0.18	2.50 ± 0.15	2.04 ± 0.12	1.76 ± 0.10	1.09 ± 0.06

Note. In the columns (from left to right): the observation, and the reflected solar flux for the seven spectral bands. The reflected fluxes have been averaged over the Earth's disk, have been averaged over 24 hr, and have been scaled to a distance of 1 au from the spacecraft and the Sun. The reflected fluxes and their standard deviations are in units of $10^{-7} \text{ W/m}^2/\mu\text{m}$. The wavelength listed in the top row is the nominal center wavelength of each filter. The wavelength below is the average wavelength, and the range below (in nm) is the full-width-at-half-maximum response to the solar spectrum (Livengood et al. 2011).

a second comet flyby (Thomas et al. 2013), photometric observations of a number of the then relatively small number of known transiting exoplanets (Christiansen et al. 2010), and observations of Earth as an exoplanet analog (Livengood et al. 2011). Those data can be used in the future to compare with exoplanets and allow an initial assessment of the habitability of the planet.

This article will investigate the change in brightness of Earth with changing phase of illumination comparable to observing a planet move through its orbit, with the outline of this paper is as follows. In Section 2, we describe the EPOXI data that we use for our analysis. In Section 3, a phase angle analysis is performed. Finally, Section 4 contains our conclusions.

2. The EPOXI Data

Within the Extrasolar Planetary Observation and Characterization part of the EPOXI mission, the Deep Space Impact spacecraft was used to observe the Earth from afar. A detailed description of the targeting, acquisition, selection, processing, and calibration of the data can be found in the paper by Livengood et al. (2011), which serves as the main reference. Other investigations have been done with subsets of the data such as azimuthal mapping of Earth's surface units and polar regions from multicolor light curves and Cowan et al. (2009, 2011); Using surface and atmospheric properties to constrain models for Earth's visible spectrum and rotational light curve (Fujii et al. 2011; Robinson et al. 2011); and using visible colors to empirically categorize Earth among the planets of our Solar System (Crow et al. 2011).

Since the publication of Livengood et al. (2011), the data has been recalibrated. The same techniques are used and the same steps are followed as described by Livengood et al. (2011),

except translated from Interactive Data Language to Python code. Note that in this paper, we include polar observations that were not reported in the paper by Livengood et al. (2011) but were used in Cowan et al. (2011). The data set used here is a calibrated second version retrieved from the NASA Planetary Data System.⁶

The measurements by the High-Resolution Instrument Visible camera (HRIV) are whole-disk images of the Earth on a 512×512 pixel subframe of the whole detector array, taken through seven spectral filters (located in a filter wheel) that have spectral widths of about 100 nm, and which are centered about 100 nm apart, from 350 to 950 nm. Livengood et al. (2011) addressed the convolution of the actual filter functions with the solar spectrum to estimate the upper and lower limits of each filter's bandwidth. Table 1 lists the characteristics of the data, and Table 2 the center wavelengths and the wavelengths that are covered by the seven filters.

Four of the filters (with nominal center wavelengths of 450, 550, 650, and 850 nm; see Table 2) were sampled every 15 minutes over a period of 24 hr, resulting in 97 measurements for each filter. The measurements at the start and the end of the 24 hour period cover the same orientation of the Earth. The other three filters (with nominal center wavelengths of 350, 750, and 950 nm; see Table 2) were sampled every 60 minutes for the same 24 hour period, resulting in 25 measurements for each filter. Here, the measurements at the start and the end also cover the same orientation of the Earth. Note that the data also includes near-infrared spectroscopy of the Earth at 1.0–4.8 μm , that was collected every two hr, but those data will be

⁶ Accessible at https://pdssbn.astro.umd.edu/holdings/dif-e-hriv-3_4-epoxi-earth-v2.0/dataset.shtml.

addressed in a future paper. The sampling strategy was designed to fit the limited spacecraft memory.

Due to the changing position of the spacecraft with respect to the Earth, there are different measurement sets. We will analyze three so-called “equatorial” observations, which were taken more or less over Earth’s equator. They will be referred to as E1, E4, and E5. We will also analyze two “polar” observations, which were taken at high latitude ($\leq 60^\circ$); one over the North pole (P1) and one over the South pole (P2). The Moon transits the Earth during E4, the Moon’s signal has been removed from the affected images. Note that P1 was acquired shortly after the northern spring equinox (i.e., on 2009 March 27–28.), thus slightly more than half of the polar cap was illuminated, while P2 was acquired only a few weeks after the southern spring equinox (i.e., on 2009 October 4–5), thus slightly more than half of the southern polar cap was illuminated. The P1 and P2 measurements have been used by Cowan et al. (2011) in their principal component analysis of the visible spectroscopy of Earth’s rotational light curve.

The first Earth image of four of the observational runs is shown in Figure 1, showing the different size of the disk depending on the geocentric distance. The spacecraft–Earth distance is 0.18 au for E1, 0.34 au for E4 and E5 (the latter image is not shown), and 0.11 au for P1 and P2. The Earth covers around half the image for E1 (there, the Earth’s diameter is 233 pixels) on a $28,000 \times 28,000$ km image. For E4 and E5, the Earth is smaller (the Earth’s diameter 129 and 126 pixels, respectively) on a $51,000 \times 51,000$ km and a $52,000 \times 52,000$ km image, respectively. For P1 and P2, the Earth takes up most of the image (the diameters are 373 and 372 pixels, respectively) on a $17,000 \times 17,000$ km and a $18,000 \times 18,000$ km image, respectively.

As can be seen, the images are not sharp as the HRIV instrument was out-of-focus, since the final design has no mechanism to focus the instrument (Klaasen et al. 2008). The lack of focus is no limitation for our application, as an ex-Earth would only be observed as a single pixel. In order to reduce the pixelated image to a single pixel value, we integrate the signals across the image. For this, first, the Earth’s centroid is determined in every image by finding the highest correlation between the image and a half disk. Then, using aperture photometry, the Earth signal is retrieved, see Figure 2. The aperture radius starts at the Earth’s edge and is increased until the collected signal no longer changes. A circular band (annulus) around the aperture is used to collect the local background signal, which is subtracted from the aperture signal. The outer radius is a factor $\sqrt[4]{2}$ times the aperture radius.

Table 2 shows the disk-integrated reflected fluxes as derived from the images with the global background level subtracted. The diurnally averaged reflected fluxes as shown in Table 2, can be compared with the values in Table 2 in Livengood et al. 2011. The values for the 950 nm band are slightly lower than the values originally published. The difference is due to calibration improvements (L. M. Feaga 2020, personal communication).

The values of the standard deviation in the data represent the signal variability due to the Earth’s rotation over the 24 hour period of each set of observations, rather than the measurement uncertainty (Figure 3). Precision uncertainty estimated from pixel-to-pixel variations in the background is negligible compared to the variability in the reflected flux that is due to Earth’s heterogeneous surface and cloud coverage over the 24

hour period over which the data was acquired. The disk-integrated reflected fluxes with their variability at the various phase angles and filters have been plotted in Figure 3, the details of which will be discussed in Section 3.

3. Phase Angle Analysis

The flux that is reflected by the Earth and that is measured by the spacecraft, depends on the coverage of the disk at the time of the observation (clouds, ocean, continents, ...) and also, strongly, on the illumination and viewing geometries, and the fraction f of the disk that is illuminated and visible, thus on the phase angle. Phase angle α is defined as the angle between the direction to the Sun and the direction to the spacecraft as measured from the center of the planet (the Sun–Earth–spacecraft angle). Note that we ignore the local variations in the angle between the directions to the Sun and the spacecraft that are due to parallaxes. At a phase angle α of 0° , the Earth’s disk that is visible for the spacecraft would be fully illuminated by the Sun, while at $\alpha = 180^\circ$, the night-side of the Earth would be in view. Table 1 shows that for our observations, phase angle α ranges from 57.7° (E1) to 86.4° (P2).

The dependence of the signal on the planetary phase angle due to the illuminated fraction f and the illumination and viewing directions of the planet needs to be taken into account when analyzing the observations and when trying to predict observations at other phase angles, since the goal of the analysis of disk-integrated data like ours is to retrieve planet characteristics like surface coverage and weather patterns. If not taken into account correctly, efforts to recover surface properties, rotational variability and weather patterns would obtain false results.

A simple model to predict the phase angle variation of the signal due to the variation in f and the illumination and viewing geometries is a model of a sphere with a Lambertian (thus isotropically), horizontally homogeneous reflecting surface. This model is an approximation because the Earth’s atmosphere has a wavelength-dependent influence on the signal such as through scattering and absorption, and including phenomena such as reddened Sun-sets, the surface reflection is wavelength dependent, and the scattering and reflection is usually nonisotropic, thus non-Lambertian. However, as a first order estimation of the Earth’s phase angle behavior, this model should allow us to gain insight into the phase angle variation without invoking detailed parameters that might not be representative for exoplanets.

The disk-integrated reflected flux of a Lambertian-reflecting, spherical planet at a phase angle α is given by (van de Hulst 1980; Stam et al. 2006; Madhusudhan & Burrows 2012)

$$j(\alpha) = \frac{r^2}{d^2} \frac{2}{3} A_s [\sin(\alpha) + (\pi - \alpha)\cos(\alpha)] \frac{1}{\pi} (\pi F_0), \quad (1)$$

where A_s is the surface albedo, r is the planet radius, d is the distance between the planet and the observer, and πF_0 is the incident solar flux measured perpendicular to the direction of incidence.

The geometric albedo A_G is defined as the flux that is reflected by the planetary body at a phase angle α of 0° divided by the flux that would have been reflected by a white, Lambertian (thus isotropically) reflecting disk of the same cross-sectional area (and with its normal pointing toward the observer) that is located at the same distance from the observer (Shepard 2017). The geometric albedo A_G of a Lambertian-

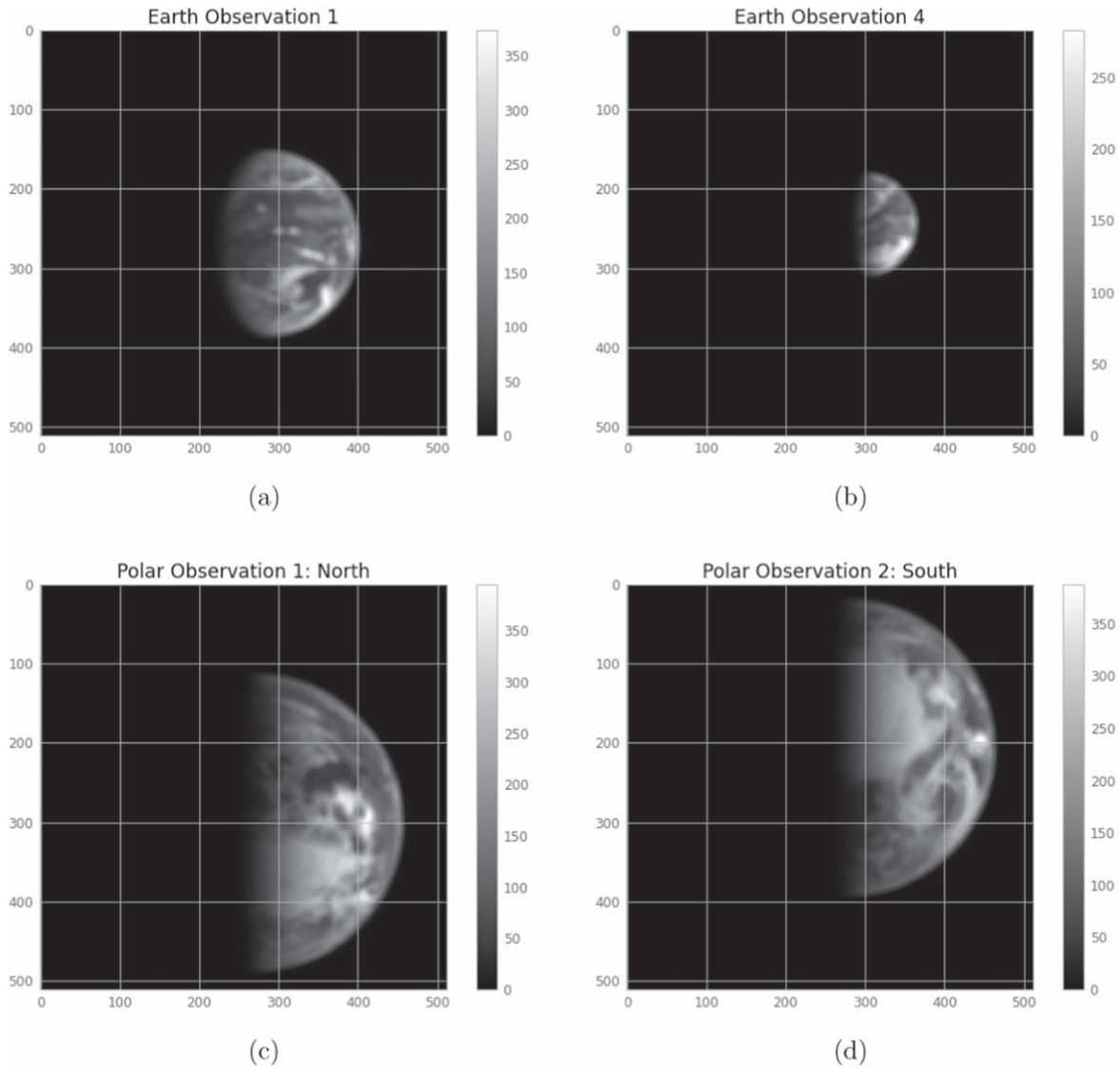


Figure 1. The first Earth image (512×512 pixel image size) of four observations at 450 nm as acquired by EPOXI’s HRIV. The legend shows the reflected solar flux in $\text{W}/(\text{m}^2 \cdot \text{sr} \cdot \mu\text{m})$. Top left: “equatorial observation 1”—E1; top right: “equatorial observation 4”—E4; bottom left: “polar observation 1”—P1; bottom right: “polar observation 2”—P2. Not shown: “equatorial observation 5”—E5, which is very similar to E4. The grid lines indicate subimages of 100×100 pixels.

reflecting planet (Equation (1)) is $\frac{2}{3}A_s$. Thus if the planetary surface is white ($A_s = 1.0$), $A_G = \frac{2}{3}$ (van de Hulst 1980).

Using the planet’s geometric albedo A_G instead of the surface albedo A_s , Equation (1) can be translated into

$$A_G = \frac{d^2 j(\alpha)}{r^2 \pi F_0} \frac{\pi}{\sin(\alpha) + (\pi - \alpha)\cos(\alpha)}, \quad (2)$$

where $j(\alpha)$ are the observational data at 1 au geocentric distance. The incoming solar flux, πF_0 , is wavelength dependent and with the $\frac{r^2}{d^2}$ factor it is scaled from the Earth’s surface to 1 au geocentric distance. We use the ASTM 2000 Standard Extraterrestrial Spectrum Reference E-490-00 (Livengood et al. 2011) for πF_0 . The geometric albedos are averaged over the 24 hr period.

The average geometric albedos of the Earth computed using Equation (2), thus assuming a Lambertian-reflecting planet (without an atmosphere), and using the data for $j(\alpha)$, in the seven spectral bands have been listed in Table 3. These albedos

range from 0.143 (E1, 950 nm) to 0.353 (P2, 350 nm). Figure 4 shows these derived geometric albedos as functions of the wavelength for the five observations. The five spectra have similar shapes with relatively high values at the shortest wavelengths, consistent with Rayleigh scattering, a smooth decrease to relatively low values around 600 nm, and increase to a local maximum at 850 nm, followed by a sharp decrease to the lowest values at 950 nm, consistent with absorption by water vapor at $\sim 1 \mu\text{m}$ (Crow et al. 2011). From the figure, it is clear that the polar observations (P1 and P2) have very similar fluxes that are significantly larger than those of the equatorial observations, which are also very similar to each other. The higher fluxes for the poles could be due to the polar ice caps that are in view of the spacecraft (see Figure 1; visible by direct inspection) or to a larger cloud coverage fraction. This will be further discussed in a later paper. The E4 and E5 values are consistently increasingly greater than E1 at larger wavelength. This is consistent with the smaller illumination fraction having more solid surface in view and less ocean surface. Note that the E1 was around equinox and the E5 observation was around

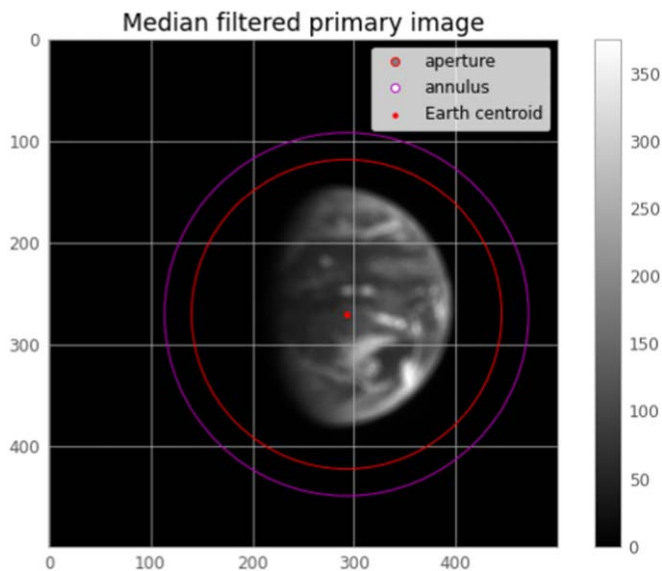


Figure 2. First E1 image (at 450 nm), showing the collection of the signal using aperture photometry. The centroid is found by finding the highest correlation with a half disk. The signal within the aperture (the inner, red, circle) is summed up and subtracted by the local background, which is the signal in the circular band (annulus) from the aperture until the outer, magenta circle.

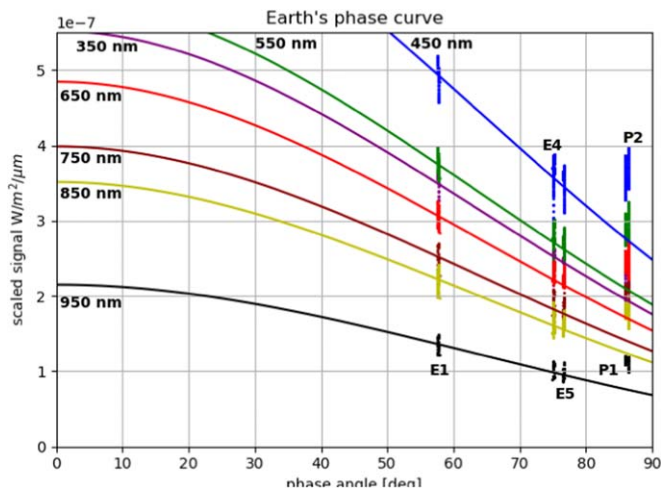


Figure 3. The reflected fluxes for the 5 observations (E1, E4, E5, P1, and P2) and the seven spectral filters (350 nm, 450 nm, 550 nm, 650 nm, 750 nm, 850 nm, and 950 nm), as listed in Table 2. The variability in the data is mainly due to the rotation of the Earth and to variations in the weather patterns during the 24 hour period over which the data is acquired. The solid curves represent the reflected fluxes as computed assuming a Lambertian-reflecting planet (without atmosphere) with (for each filter band) a geometric albedo A_G derived from the E1 data. Note that while these curves fit not only the E1 data, they also fit the E4 and E5 data, while the P1 and P2 data are clearly higher than the curves.

solstice, so seasonal effects could also cause a difference. Nonetheless, the equatorial observations are quite similar to each other.

The geometric albedos listed in Table 3 and shown in Figure 4 are smaller than the classical (visible v-band, $0.549 \mu\text{m}$) geometric albedo of 0.434.⁷ Lesser values for the Earth’s geometric albedo have been published such as 0.2

(Mallama 2009), 0.367 (visible $0.554 \mu\text{m}$; Harris 1961), 0.15–0.45 (for $0.5\text{--}1.0 \mu\text{m}$; Madden & Kaltenecker 2018), <0.1 (for $0.2\text{--}2.0 \mu\text{m}$, half illumination of Earth; Schwieterman et al. 2018), and 0.15 (Robock 1980). They are closer to the observations but they are either too low or too high due to the observations wavelength dependence or due to the higher polar observations. For the equatorial observations, the values are for most wavelengths just too high. Mallama et al. (2017) reports geometric albedo values for the Johnson–Cousins system or Sloan system. In this article values range from 0.392 (R_C , $0.641 \mu\text{m}$) to 0.688 (U , $0.360 \mu\text{m}$) for Johnson–Cousins and from 0.388 (r' , $0.616 \mu\text{m}$) to 0.722 (u' , $0.355 \mu\text{m}$) for Sloan. These values are calculated using the same EPOXI data presented here but a different phase function is used to extrapolate to zero phase angle. They use the (steeper) phase function for the “realistic clouds” case plotted in Figure 7 of Tinetti et al. (2006b) and therefore they have higher values than the ones reported here. The geometric albedo values presented here are not necessarily an accurate representation of Earth’s geometric albedo. In fact, the Lambertian scattering model cannot fully represent Earth’s phase function, since it cannot account for the difference in retrieved geometric albedo from the polar data compared to the equatorial data, even though the geometry at the subsolar point must be the same for both models and thus should represent the same albedo. The values retrieved here serve as a means to extrapolate the phase curve to a limited extent beyond the modest range of phase angle directly observed and to compare the degree of consistency between the differing phase angle observations. These observations also provide a cautionary case study for future retrievals from actual exoplanets.

It is important to note that the phase angle dependence of the flux that is reflected by a planet with a Lambertian-reflecting surface and no atmosphere is generally less steep than that of a planet with an atmosphere. In particular, for a given geometric albedo A_G , and at $\alpha = 90^\circ$, the flux of a Lambertian planet with a gaseous atmosphere is only 75% of that of a Lambertian planet without atmosphere, and at $\alpha = 60^\circ$, it is 78% (Stam et al. 2006). This would mean that a geometric albedo derived assuming a Lambertian-reflecting planet would be an underestimation compared to the real value. A model comparison to show the effect of the Lambertian model assumption is shown in Appendix.

As a next step, we used the wavelength dependent geometric albedos that we derived from the E1 data (the first row of Table 3) and computed the phase curves for a Lambertian-reflecting planet (see Equation (1)), to allow a comparison with the data taken at the different phase angles. The comparison is shown in Figure 3. The phase curves based on the data from the E1 observations fit the other two equatorial observations, E4 and E5, very well, confirming the similarity between the three equatorial observations that we noted before when inspecting the geometric albedos (thus at a phase angle of 0° , Figure 4) over the whole phase angle range. The phase curves also confirm that the polar data (P1 and P2) are very different from the equatorial data. In particular, the reflected fluxes are much higher. The absolute differences between the hence computed phase curves and the observations data are listed in Table 4.

Table 4 contains the absolute mean differences in flux (in the table “mean deviation”) between all data points that were taken during the 24 hour period over which the data for each observation was acquired (25 for the 350, 750, and 950 nm

⁷ Taken from <https://nssdc.gsfc.nasa.gov/planetary/factsheet/earthfact.html>, acquired on 01/12/2020.

Table 3

The 24 hr Averaged Geometric Albedos A_G (Computed at $\alpha = 0^\circ$ Assuming a Lambertian-reflecting planet) and their Standard Deviations for the Five Observations (E1, E4, E5, P1, and P2) at the Seven Spectral Bands

Obs.	α	Central Filter Wavelengths			
		350 nm	450 nm	550 nm	650 nm
E1	57.7°	0.294 ± 0.010	0.229 ± 0.009	0.176 ± 0.007	0.167 ± 0.007
E4	75.1°	0.289 ± 0.017	0.231 ± 0.015	0.181 ± 0.010	0.173 ± 0.009
E5	76.6°	0.291 ± 0.013	0.234 ± 0.012	0.183 ± 0.008	0.174 ± 0.006
P1	85.9°	0.343 ± 0.016	0.296 ± 0.015	0.240 ± 0.010	0.236 ± 0.008
P2	86.4°	0.353 ± 0.015	0.312 ± 0.015	0.255 ± 0.016	0.246 ± 0.015
Mean P/E		1.196 ± 0.050	1.314 ± 0.061	1.375 ± 0.064	1.407 ± 0.061

Obs.	α	Central Filter Wavelengths		
		750 nm	850 nm	950 nm
E1	57.7°	0.172 ± 0.009	0.188 ± 0.011	0.143 ± 0.009
E4	75.1°	0.180 ± 0.011	0.199 ± 0.014	0.149 ± 0.011
E5	76.6°	0.182 ± 0.009	0.201 ± 0.013	0.148 ± 0.011
P1	85.9°	0.248 ± 0.007	0.271 ± 0.009	0.213 ± 0.007
P2	86.4°	0.251 ± 0.015	0.270 ± 0.016	0.207 ± 0.012
Mean P/E		1.402 ± 0.064	1.380 ± 0.070	1.432 ± 0.075

Note. The last row shows the mean P/E, which is the ratio of the mean polar albedo (P1, P2) and the mean equatorial albedo (E1, E4, and E5). The uncertainty of this ratio is found by using propagation of error.

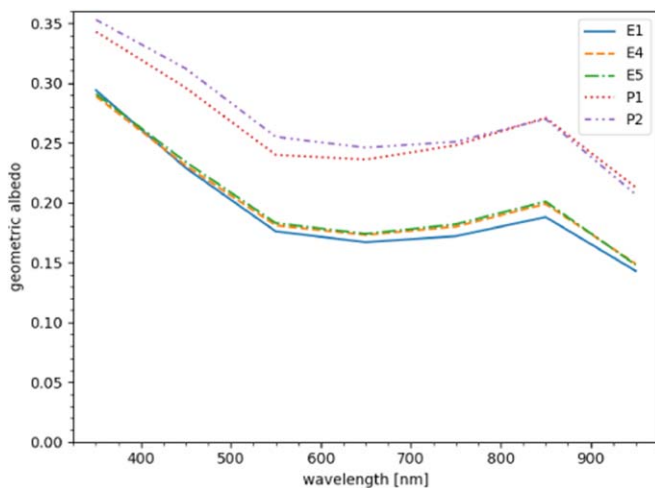


Figure 4. The geometric albedo's A_G as functions of the central filter wavelengths (350, 450, 550, 650, 750, 850, and 950 nm) as derived from the measurements E1, E4, E5, P1, and P2 (see Table 2) assuming a Lambertian-reflecting planet (without atmosphere).

filters; and 97 for the 450, 550, 650, and 850 nm filters) and the computed value of the phase curve for the Lambertian-reflecting planet at the phase angle pertaining to the observation (cf. Table 1). Because the Earth rotates within the 24 hour period and because local weather patterns, in particular clouds, change over time, the mean deviation also reflects these actual variations in time. The deviation is larger for the polar observations as these are brighter than the equatorial observations and are thus not fitted by the phase curve computed for E1.

Table 4 also contains the standard deviation of the mean deviation, which also reflects the actual variations in time, such as the Earth's rotation. The standard error of the mean is given to assess the confidence in the mean. The values are given for

Equatorial observation 1 (E1) as well, even though those data were used to calculate the phase curves. It can be seen that the mean errors for E4 and E5 are close to those for E1. Thus we can be confident that the differences between the data points of E4 and E5 and the phase curves are also due to time variations, such as the Earth's rotation. As the values for the standard deviation are mainly driven by time variations such as due to Earth's rotation, they are very similar for the equatorial observations as they cover the same region of the Earth (apart from the clouds).

For the polar observations, the mean errors are larger than the standard deviations indicating that there is indeed an offset in the data that is not due to the Earth's rotation, i.e., the polar observations are significantly brighter. The standard deviations for the polar data are similar to those for the equatorial data, indicating that the Earth's rotation and cloud variations have a similar effect, except for the longest wavelengths in the north polar observations (P1). Those standard deviations are smaller than those for P2, which can also be seen in Figure 3, especially for the 950 nm data points of P1. This would indicate that at the time of observations ('09 March 27–28 for P1, see Table 1), the north polar region appeared to be more rotationally symmetric than the south polar region at the time of observation ('09 October 4–5 for P2, see Table 1). This is consistent with direct inspection of North American and Asian land masses in the images.

Finally, Table 4 also contains the standard errors of the mean, in order to prove that the limited number of data points (25 images for the 350, 750, and 950 nm filters; and 97 images for the other filters) do not undermine the above conclusions. They are all significantly smaller than the mean error, showing that the latter is relatively certain.⁸ Therefore, the mean errors are expected to remain smaller (for E1, E4, and E5) and larger (for P1 and P2) than the standard deviations even when more

⁸ One could create a confidence interval for the mean error by adding and subtracting the standard error of the mean to and from the mean error.

Table 4

The Mean Deviation (seen in Figure 3) between the Observational Data and the Phase Curves of a Lambertian-reflecting Planet Model with the Wavelength-dependent 24 hr Averaged Geometric Albedos Derived of Observation E1 (using Equation (2)) Together with the Standard Deviation and the Standard Error of the Mean

Wavelength [nm]	Mean deviation [W/m ² /μm]	Standard Deviation [W/m ² /μm]	Standard Error of the Mean [W/m ² /μm]
Equatorial Observation 1 (E1)			
350	1.06e-8	1.20e-8	2.5e-9
450	1.75e-8	1.98e-8	2.0e-9
550	1.24e-8	1.41e-8	1.4e-9
650	1.09e-8	1.23e-8	1.3e-9
750	1.09e-8	1.27e-8	2.6e-9
850	1.07e-8	1.28e-8	1.3e-9
950	0.75e-8	0.85e-8	1.7e-9
Equatorial Observation 4 (E4)			
350	1.06e-8	1.45e-8	3.0e-9
450	1.94e-8	2.33e-8	2.4e-9
550	1.34e-8	1.56e-8	1.6e-9
650	1.15e-8	1.15e-8	1.2e-9
750	1.25e-8	1.14e-8	2.3e-9
850	1.26e-8	1.18e-8	1.2e-9
950	0.73e-8	0.73e-8	1.5e-9
Equatorial Observation 5 (E5)			
350	0.90e-8	1.09e-8	2.2e-9
450	1.84e-8	1.77e-8	1.8e-9
550	1.33e-8	1.12e-8	1.1e-9
650	1.07e-8	0.78e-8	0.8e-9
750	1.29e-8	0.95e-8	1.9e-9
850	1.36e-8	1.04e-8	1.1e-9
950	0.67e-8	0.69e-8	1.4e-9
Polar Observation 1 (P1): North			
350	3.28e-8	1.08e-8	2.2e-9
450	8.23e-8	1.78e-8	1.8e-9
550	7.66e-8	1.15e-8	1.2e-9
650	7.12e-8	0.79e-8	0.8e-9
750	6.27e-8	0.61e-8	1.2e-9
850	5.48e-8	0.57e-8	0.6e-9
950	3.76e-8	0.37e-8	0.8e-9
Polar Observation 2 (P2): South			
350	3.66e-8	0.96e-8	2.0e-9
450	9.67e-8	1.76e-8	1.8e-9
550	9.04e-8	1.82e-8	1.9e-9
650	7.86e-8	1.52e-8	1.6e-9
750	6.28e-8	1.17e-8	2.4e-9
850	5.19e-8	1.04e-8	1.1e-9
950	3.29e-8	0.65e-8	1.3e-9

Note. The Earth’s rotation causes a variation in the signal, therefore there is a nonzero deviation even for E1.

data would be added (note that the standard errors of the mean are somewhat larger for the filters with less observations, i.e., 350, 750, and 950 nm, than for the other filters).

The observations can also be compared with different phase curves. Tinetti et al. (2006b) presents a phase light curve for the 0.5–0.9 μm wavelength range in Figure 7(a) (the general Earth model is presented in Tinetti et al. 2006a) that can be used. The albedos of the equatorial observations (of the relevant

wavelength filters) match the “realistic clouds” model closely. They are slightly higher than the model but this is hard to assess with the low sampling rate of the model lines. The polar observations clearly do not agree with the “realistic clouds” model. They are closer to the “strato-cumulus” and “alto-stratus” model lines (low and middle clouds; Tinetti et al. 2006b), although slightly lower than those lines. They are lower because the model lines are for a fully cloud-covered disk-averaged spectra. From visual inspection of Figure 1, it can be seen that the EPOXI polar observations have more clouds in view than the equatorial observations. The mid-latitudes are more cloudy than the tropics (Cowan et al. 2011), which explains why the polar observations have higher albedo values than the Tinetti et al. 2006b “realistic clouds” model due to the increased solid angle presented in the field of view. Modeling has been done, which confirms that the polar observations have slightly higher cloud coverage, this work will be published later.

4. Conclusion

The EPOXI mission imaged the Earth’s full disk from afar and at five occasions: three equatorial and two polar views (the latter included one north and one south pole observation) at visible wavelengths (from 0.3 to 1.0 μm). The images were taken with the High-Resolution Instrument Visible onboard NASA’s Deep Impact spacecraft and vary in distance to the Earth and in phase angle at the time of observation. The complete and calibrated version of the visible data is presented in this article along with a phase angle analysis.

Additional near-infrared data that was also acquired is not used in this article but has been presented before by Livengood et al. (2011) and that description serves as our main reference. A detailed description of the targeting, acquisition, selection, and processing (including calibration) along with a presentation of the old data (newly calibrated data is used in this article) can be found in that paper.

The Earth images have been taken through seven spectral filters centered 100 nm apart, covering wavelengths from 350 to 950 nm, and they were sampled every 15 minutes for four filters (450, 550, 650, and 850 nm) and every 60 minutes for the other three filters (350, 750, and 950 nm) each over a period of 24 hr. Using aperture photometry, disk-integrated Earth fluxes are retrieved for every filter, averaged over 24 hr and scaled to a 1 au range from the spacecraft. These fluxes are compared with a Lambertian-reflecting planet model (see Equation (1)), which is often used as a first order assumption or reference as comparison (Fujii et al. 2010, 2011; Cowan et al. 2009, 2011; Robinson et al. 2011).

The fluxes of one of the equatorial observations are used to determine the geometric albedo of the Earth at every filter, assuming a Lambertian-reflecting planet (thus without scattering atmosphere), and to analyze the phase angle behavior for the other four observations. This approach allows us to match the other two equatorial observations over the phase angles, confirming the similarity between the three observations (recall that each set of observations was integrated over 24 hr, thus each covering a whole rotation of the Earth), but it underestimates the geometric albedos derived from the two polar observations. That could be due to the ice that is visible in those two observations.

As a next step, we derived the geometric albedos for all the observations and the seven wavelength filters, again assuming a

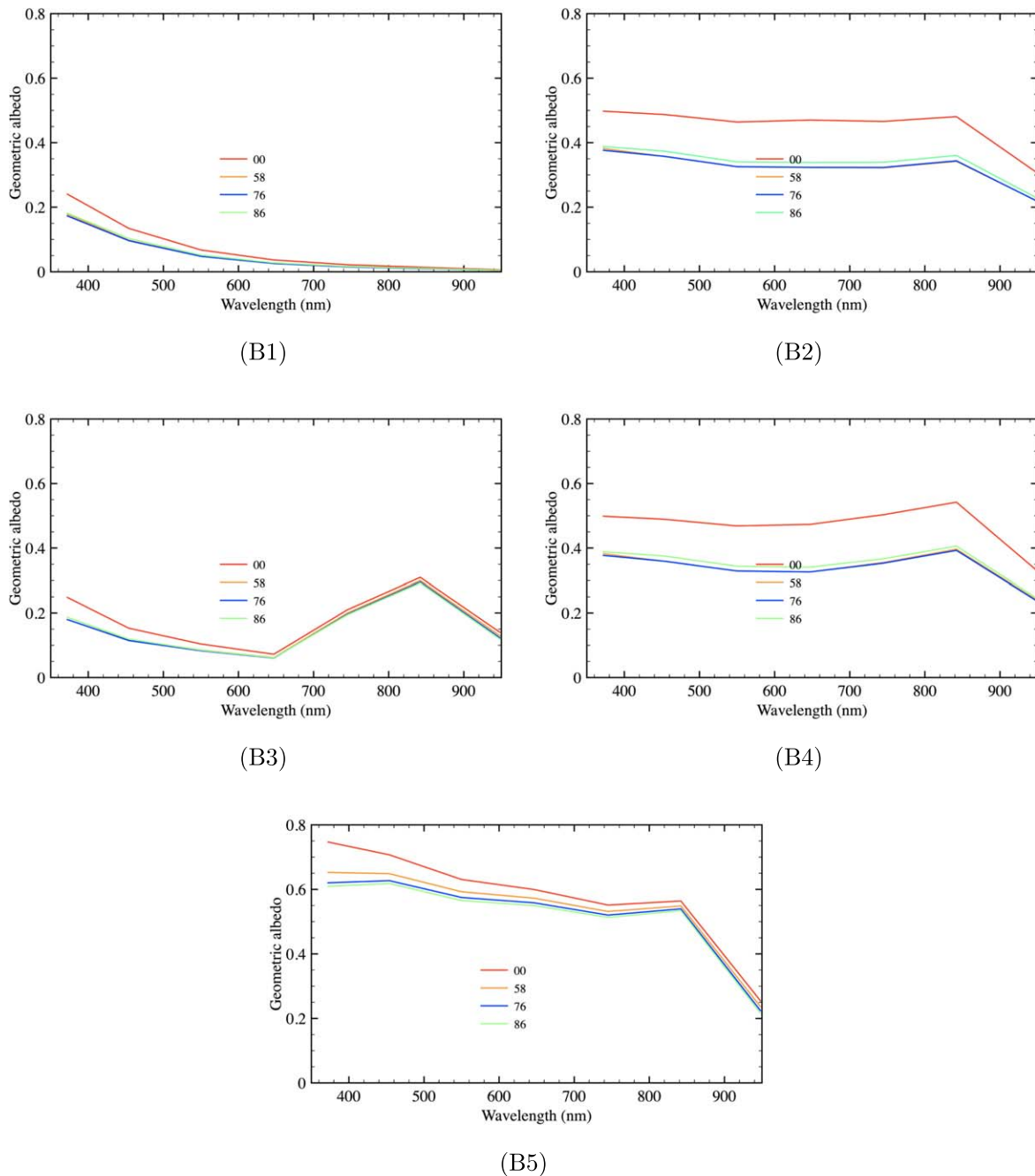


Figure 5. Geometric albedo of models (Stam 2008) over wavelength for various phase angles, applying the inverse Lambertian phase function to retrieve geometric albedo. The zero phase angle model is the correct geometric albedo and the difference with the other model lines shows the effect of using a Lambertian phase function to retrieve the geometric albedo. B1 has ocean surface albedo without cloud and B2 with clouds. A vegetation surface without cloud is shown in B3 and with clouds in B4. B5 is an ice surface without clouds.

Lambertian-reflecting planet (thus without scattering atmosphere; see Table 3). The hence derived geometric albedos range from 0.143 to 0.353 and are, as expected, wavelength dependent. The albedos derived from the polar observations are distinctly higher than those from the equatorial observations, with the difference being larger for longer wavelengths, where the influence of the atmosphere is smaller. The geometric albedo values that we retrieve are smaller than the classic (visible v -band, $0.549 \mu\text{m}$) geometric albedo value of

0.434.⁹ In this article values for geometric albedo range from 0.392 (R_C , $0.641 \mu\text{m}$) to 0.688 (U , $0.360 \mu\text{m}$) for Johnson–Cousins and from 0.388 (r' , $0.616 \mu\text{m}$) to 0.722 (u' , $0.355 \mu\text{m}$) for Sloan. These values are calculated using the same EPOXI data presented here but a different phase function is used to extrapolate to zero phase angle. They use the (steeper) phase function for the “realistic clouds” case plotted in Figure 7 of Tinetti et al. (2006b). Lower estimates of 0.2 (Mallama 2009), 0.15–0.45 (for $0.5\text{--}1.0 \mu\text{m}$; Madden & Kaltenecker 2018) are

⁹ Taken from <https://nssdc.gsfc.nasa.gov/planetary/factsheet/earthfact.html>, acquired on 01/12/2020.

closer to the observations but they are either too low or too high due to the observations wavelength dependence or due to the higher polar observations. For the equatorial observations, the values are for most wavelengths just too high. Mallama et al. (2017) reports geometric albedo values for the Johnson–Cousins system or Sloan system. In this article values range from 0.392 (R_C , $0.641 \mu\text{m}$) to 0.688 (U , $0.360 \mu\text{m}$) for Johnson–Cousins and from 0.388 (r' , $0.616 \mu\text{m}$) to 0.722 (u' , $0.355 \mu\text{m}$) for Sloan. These values are calculated using the same EPOXI data presented here but a different phase function is used to extrapolate to zero phase angle. They use the (steeper) phase function for the “realistic clouds” case plotted in Figure 7 of Tinetti et al. (2006b), and therefore they have higher values than the ones reported here. Since the geometric albedo is essential to estimating the energy budget for a planet, it is essential to consider the whole range of possible values in estimating planetary surface temperature. The geometric albedo values presented here are not necessarily an accurate representation of Earth’s geometric albedo. In fact, the Lambertian scattering model cannot fully represent Earth’s phase function, since it cannot account for the difference in retrieved geometric albedo from the polar data compared to the equatorial data, even though the geometry at the subsolar point must be the same for both models and thus should represent the same albedo. The values retrieved here serve as a means to extrapolate the phase curve to a limited extent beyond the modest range of phase angle directly observed and to compare the degree of consistency between the differing phase angle observations. These observations also provide a cautionary case study for future retrievals from actual exoplanets. Additionally, the Lambertian model assumption with no atmosphere causes an underestimation of the geometric albedo. Stam et al. (2006) found that for a given geometric albedo A_G , and at 90° phase angle, the flux of a Lambertian planet with a gaseous atmosphere is only 75% of that of a Lambertian planet without atmosphere, and at 60° phase angle, it is 78%. The retrieved values of geometric albedo will be used in a future paper, which focuses on Earth modeling.


More full disk observations of the Earth, covering a wider and more complete phase angle range, would help a more extended analysis of the Earth’s phase curve. Other distant space observations of the Earth, such as from the Mars Global Surveyor (Christensen & Pearl 1997), or the MESSENGER mission when it started its trajectory to Mercury (García Muñoz 2015) can be used for a similar model comparison and extent the understanding of Earth’s appearance as an exoplanet and with that our future understanding of what can be retrieved from single pixel observations of real exoplanets such as those to be acquired planned space telescopes for the direct imaging of terrestrial-type exoplanets, like Habex (Gaudi et al. 2020) and LUVOIR (The LUVOIR Team 2019).

This article serves as master thesis at TU Delft, the relevant personnel that allows for this graduation is gratefully acknowledged. Appreciative acknowledgments to the EPOXI team especially for Mike A’Hearn for these observations and to NASA for making the data publicly available.

Appendix Additional Model Plots

The geometric albedo of a model (using the Stam 2008 model) at phase angle zero is compared to the geometric albedo models at the observational phase angle, see Figure 5. The geometric albedo of the nonzero phase angles is retrieved by applying the inverse Lambertian phase function (see Equation (2)). This is done to assess the effect of the Lambertian model assumption. The zero phase angle model has the correct values of geometric albedo while the other phase angles have lower values as the atmosphere is not included in the Lambertian model. If the model has no clouds the difference is relatively small because only at shorter wavelength the atmosphere contributes significantly. At longer wavelengths, the Lambertian-reflecting surface is clearly in view and the assumption gets better for all phase angles. For the cloudy planets, the atmosphere contributes at all wavelengths, and the difference is larger over all wavelengths.

ORCID iDs

Roderick De Cock  <https://orcid.org/0000-0002-5444-6185>
 Timothy A. Livengood  <https://orcid.org/0000-0002-9947-4075>
 Daphne M. Stam  <https://orcid.org/0000-0003-3697-2971>
 Carey M. Lisse  <https://orcid.org/0000-0002-9548-1526>

References

- Aschbacher, J., & Milagro-Pérez, M. P. 2012, *RSEnv*, 120, 3
 Blume, W. H. 2005, *SSRv*, 117, 23
 Bryson, S., Kunimoto, M., Kopparapu, R. K., et al. 2020, *AJ*, 161, 36
 Christensen, P. R., & Pearl, J. C. 1997, *JGRE*, 102, 10875
 Christiansen, J. L., Ballard, S., Charbonneau, D., et al. 2010, *ApJ*, 726, 94
 Cowan, N. B., Agol, E., Meadows, V. S., et al. 2009, *ApJ*, 700, 915
 Cowan, N. B., Robinson, T., Livengood, T. A., et al. 2011, *ApJ*, 731, 76
 Crow, C. A., McFadden, L. A., Robinson, T., et al. 2011, *ApJ*, 729, 130
 Fujii, Y., Kawahara, H., Suto, Y., et al. 2011, *ApJ*, 738, 184
 Fujii, Y., Kawahara, H., Suto, Y., et al. 2010, *ApJ*, 715, 866
 García Muñoz, A. 2015, *IJAsB*, 14, 379
 Gaudi, B. S., Seager, S., Mennesson, B., et al. 2020, arXiv:2001.06683
 Harris, D. L. 1961, in *Planets and Satellites*, ed. G. P. Kuiper & B. M. Middlehurst (Chicago, IL: Univ. of Chicago Press), 272
 Hearty, T., Song, I., Kim, S., & Tinetti, G. 2009, *ApJ*, 693, 1763
 Kansakar, P., & Hossain, F. 2016, *SpPol*, 36, 46
 Klaasen, K. P., A’Hearn, M. F., Baca, M., et al. 2008, *RSci*, 79, 091301
 Livengood, T. A., Deming, L. D., A’Hearn, M. F., et al. 2011, *AsBio*, 11, 907
 Madden, J., & Kaltenecker, L. 2018, *AsBio*, 18, 1559
 Madhusudhan, N., & Burrows, A. 2012, *ApJ*, 747, 25
 Mallama, A. 2009, *Icar*, 204, 11
 Mallama, A., Krobusek, B., & Pavlov, H. 2017, *Icar*, 282, 19
 Mettler, J.-N., Quanz, S. P., & Helled, R. 2020, *AJ*, 160, 246
 Pfeifer, M., Disney, M., Quaipe, T., & Marchant, R. 2012, *Glob. Ecol. Biogeogr.*, 21, 603
 Robinson, T. D., Meadows, V. S., Crisp, D., et al. 2011, *AsBio*, 11, 393
 Robock, A. 1980, *MWRv*, 108, 267
 Schwieterman, E. W., Kiang, N. Y., Parenteau, M. N., et al. 2018, *AsBio*, 18, 663
 Shepard, M. K. 2017, *Introduction to Planetary Photometry* (Cambridge: Cambridge Univ. Press)
 Stam, D. M. 2008, *A&A*, 482, 989
 Stam, D. M., De Rooij, W. A., Cornet, G., & Hovenier, J. W. 2006, *A&A*, 452, 669
 The LUVOIR Team 2019, arXiv:1912.06219
 Thomas, P., A’Hearn, M. F., Veverka, J., et al. 2013, *Icar*, 222, 550
 Tinetti, G., Meadows, V. S., Crisp, D., et al. 2006a, *AsBio*, 6, 34
 Tinetti, G., Meadows, V. S., Crisp, D., et al. 2006b, *AsBio*, 6, 881
 van de Hulst, H. 1980, *Multiple Light Scattering* (New York: Academic)